

Search for the second forbidden beta decay of ${}^8\text{B}$ to the ground state of ${}^8\text{Be}$

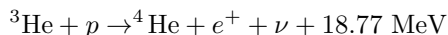
M. K. Bacrania,* N. M. Boyd,† R. G. H. Robertson, and D. W. Storm
*Center for Experimental Nuclear Physics and Astrophysics,
Physics Department, University of Washington, Seattle, WA 98195*
(Dated: October 15, 2018)

A significant decay branch of ${}^8\text{B}$ to the ground state of ${}^8\text{Be}$ would extend the solar neutrino spectrum to higher energies than anticipated in the standard solar models. These high-energy neutrinos would affect current neutrino oscillation results and also would be a background to measurements of the hep process. We have measured the delayed alpha particles from the decay of ${}^8\text{B}$, with the goal of observing the two 46-keV alpha particles arising from the ground-state decay. The ${}^8\text{B}$ was produced using an in-flight radioactive beam technique. It was implanted in a silicon PIN-diode detector that was capable of identifying the alpha-particles from the ${}^8\text{Be}$ ground state. From this measurement we find an upper limit (at 90% confidence level) of 7.3×10^{-5} for the branching ratio to the ground state. In addition to describing this measurement, we present a theoretical calculation for this branching ratio.

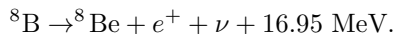
PACS numbers: 23.40.-s, 23.40.Bw, 23.60.+e, 26.65.+t, 27.20.+n

I. INTRODUCTION

There have been several experiments [1, 2, 3] done recently to measure the alpha-particle spectrum following the allowed (2^+ to 2^+) beta decay of ${}^8\text{B}$ to the broad first excited state at 3 MeV in ${}^8\text{Be}$. The neutrinos from this decay provide the signal for solar neutrino measurements, such as SNO and SuperKamiokande, and precise knowledge of their spectrum at creation, combined with accurate measurements in the solar neutrino detectors, is important for understanding neutrino oscillations. The only higher energy neutrinos from the Sun come from the hep [4] process (weak capture of a proton by ${}^3\text{He}$ producing $e^+ + \nu$), expected to be at a rate roughly 10^{-3} of the ${}^8\text{B}$ neutrinos, and from the second forbidden (2^+ to 0^+) decay of ${}^8\text{B}$ to the ground state of ${}^8\text{Be}$. Specifically these reactions are



and



An ft value for the latter decay, estimated using $\log_{10} ft = 13.3$ obtained from the 2^+ to 0^+ decay of ${}^{36}\text{Cl}$, suggests the ${}^8\text{B}$ 2^+ to 0^+ decay should have a branching ratio of order only 10^{-7} . The ${}^8\text{B}$ decay has an unusually large energy, and second-forbidden decays should have an extra factor of k^2 (k is the momentum transfer to the leptons) in their decay rate. Comparing the square of the endpoint energy for ${}^8\text{B}$ with that for ${}^{36}\text{Cl}$ suggests an additional factor of 570 in the rate for the second forbidden decay of ${}^8\text{B}$. This rate would correspond to

a $\log_{10} ft$ of 10.5, a value still in the expected range for second-forbidden transitions. The corresponding branching ratio would be 3×10^{-5} . If the branching ratio were as large as about 1%, it would contribute significantly to the neutrino spectrum observed at SNO.

Decay to the ground state of ${}^8\text{Be}$ is difficult to measure, since that state decays to two alpha particles producing only 92 keV. We are unaware of previous attempts to measure this branch. Published estimates range from 3×10^{-6} [5] to $O(10^{-4})$ [6, 7]. The latter estimate includes only the vector contribution to the second-forbidden decay. In this paper we describe the technique of our measurement, give the result, and present theoretical calculations based on the shell model and on measured gamma-ray transition matrix elements.

II. EXPERIMENT

We made a ${}^8\text{B}$ beam using an in-flight production technique. The ${}^8\text{B}$ were implanted in a silicon detector that was capable of measuring the energy from the delayed alpha decay of the ${}^8\text{Be}$ ground state, as well as from most of the spectrum of delayed alpha decay of the ${}^8\text{Be}$ first excited state. The decays were tagged by detecting the decay positrons in a scintillator. The silicon detector was calibrated using back scattered α particles of known energy and also using delayed alpha decays of implanted ${}^{12}\text{N}$.

A. Radioactive beams

The ${}^8\text{B}$ for implantation in the detector was made using the ${}^3\text{He}({}^6\text{Li}, {}^8\text{B})n$ reaction. A 32-mm-diameter gas cell was located at the focal point of the analyzing magnet of the University of Washington Tandem accelerator. This gas cell had entrance and exit windows of $2.5\text{-}\mu\text{m}$ Havar [8] and contained ${}^3\text{He}$ at about 0.6 bar. The inci-

*Presently at Nuclear Safeguards Science and Technology, Los Alamos National Laboratory, Los Alamos, NM 87544

†Presently at Department of Physics and Astronomy, University of British Columbia, Vancouver, BC V6T 1Z1

dent beam was 24-MeV ${}^6\text{Li}$, which, after accounting for energy loss in the windows and gas, produced ${}^8\text{B}$ in the forward direction with an energy centered at 15.5 MeV and a spread of 1.1 MeV, resulting from energy loss in the gas.

The beam transport following the analyzing magnet consisted of a 30° switching magnet followed by a quadrupole doublet. These elements are normally used to focus the analyzed beam from the accelerator onto the target in the scattering chamber. For the present experiment we had to optimize the capture and transport of the radioactive beam through the 20-mm aperture for our detector, which was located at the target position in the scattering chamber. We found, using TRANSPORT [9] and TURTLE [10], that this could be done by first tuning the beamline following the gas cell appropriately for transport of a straight-going monoenergetic beam of the desired magnetic rigidity, and then by increasing the quadrupole strength by about 10%. The energy acceptance of this system was only about 2%, which is less than the energy spread resulting from the gas cell, so there was no reason to have either a bigger cell or denser gas. We tuned the radioactive beam transport elements by tuning first a 7.44-MeV ${}^6\text{Li}^{3+}$ beam (matching the 15.5-MeV ${}^8\text{B}^{5+}$ radioactive beam in magnetic rigidity) through a small aperture. Then, while irradiating the gas cell with the 24-MeV ${}^6\text{Li}$ beam, we would monitor the ${}^8\text{B}$ implantation rate and increase the quadrupole current to maximize the rate. We also swept the switching magnet field, which we monitored with a Hall probe, to make sure we were accepting the central energy from the gas cell.

As the rigidity of the primary beam is higher than that of the radioactive beam, degraded primary beam is a serious contaminant. In order to minimize degradation of the primary beam after the analyzing magnet, we regulated the accelerator voltage with the Generating Volt Meter Regulator [11] and completely retracted the beam regulation slits located downstream of the analyzing magnet. Particular attention had to be paid to the beam tuning, in order to minimize the amount of beam striking other limiting apertures in the beamline.

In addition to the ${}^8\text{B}$ beam, we produced a ${}^{12}\text{N}$ beam for calibration of the silicon detector. This beam was made using the ${}^3\text{He}({}^{10}\text{B}, {}^{12}\text{N})\text{n}$ reaction, with a 35-MeV ${}^{10}\text{B}$ beam, producing 24.2-MeV ${}^{12}\text{N}^{7+}$, in an analogous manner. The ${}^{12}\text{N}$ energy was chosen to produce the same implantation depth for the ${}^{12}\text{N}$ as for the ${}^8\text{B}$. The choice of the ${}^{12}\text{N}$ charge state was determined by the background, because the most-probable charge state of ${}^{12}\text{N}$, $6+$, was too close in rigidity to the ${}^{10}\text{B}$ primary beam. Using the coincidence with the scintillator, we were able to tag about $3 - 5$ ${}^8\text{B}$ per second with 170 to 330 particle nA of ${}^6\text{Li}$, and about $0.5 - 1$ ${}^{12}\text{N}$ per second with 50 to 100 particle nA of ${}^{10}\text{B}$. For the ${}^8\text{B}$ beam, the background in the silicon detector, primarily consisting of degraded ${}^6\text{Li}$ from the primary beam, was $0.6 - 1$ kHz. For the ${}^{12}\text{N}$ beam, the degraded ${}^{10}\text{B}$ background was 2 kHz. This

background rate in our detector set an intensity limit for the primary beam.

B. Detector

The detector assembly consisted of a $500\text{-}\mu\text{m}$ thick by 18-mm square Hamamatsu S-3204-06 PIN diode [12], in front of which was a 51-mm cube of Bicron-400 scintillator with a 20-mm-diameter hole on the beam axis. A lead shield 6.4-mm thick with a 17-mm-diameter aperture was placed in front of the scintillator, and the scintillator was coupled on the side to a photomultiplier tube. This thickness of lead was sufficient to absorb positrons from decaying ${}^8\text{B}$ that stopped on it. Ions that passed through the lead aperture would stop in the PIN diode, and were not able to hit the sides of the hole in the scintillator.

The 15-MeV ${}^8\text{B}$ ions were implanted approximately 20 μm into the silicon, and about 20% of the decays produced positrons that would enter the scintillator, tagging the decay. In order to minimize distortions in the α -particle spectrum from positron energy deposition, the scintillator detector was placed in front of the silicon detector, thus minimizing the track length of the tagged positrons in the silicon detector. Tagging with positrons that passed through the silicon detector was not practical, as their energy deposition would be larger than the energy from the decay from the ${}^8\text{B}$ ground state. Indeed, as is discussed in section IID 2, positrons that scatter through large angles affect the efficiency of the detection. The PIN diode was mounted on a custom charge-sensitive preamplifier [13] built on a 5-cm-square circuit board. The preamp and detector were cooled by a thermoelectric cooler coupled to a 19-mm-wide and 3-mm-thick copper strip that ran the height of the preamplifier circuit board. This assembly is shown in Fig. 1.

When cooled to 10°C , the measured leakage current of a new PIN diode was typically 10 – 12 nA. The resolution (FWHM) was 7.8 keV for 81-keV gamma rays, and a threshold about 30 keV was practical. During experimental runs, the reverse current would rise to 30 – 60 nA after 2 weeks of irradiation, at which point the resolution would decrease to approximately 10 keV at 81 keV.

C. Electronics and data acquisition

The photomultiplier on the scintillation detector produced both a timing and a pulse-height signal. The timing signal started a time to amplitude converter (TAC). The output of the charge-sensitive preamplifier for the silicon diode detector was split into two channels, each with an Ortec 572 amplifier. The maximum range of the *high gain* channel corresponded to about 1 MeV, while the maximum observable energy in the *low gain* channel was 8 MeV. The two unipolar signals were digitized, as was the pulse-height signal from the scintillator. The bipolar outputs of the amplifiers for the silicon detec-

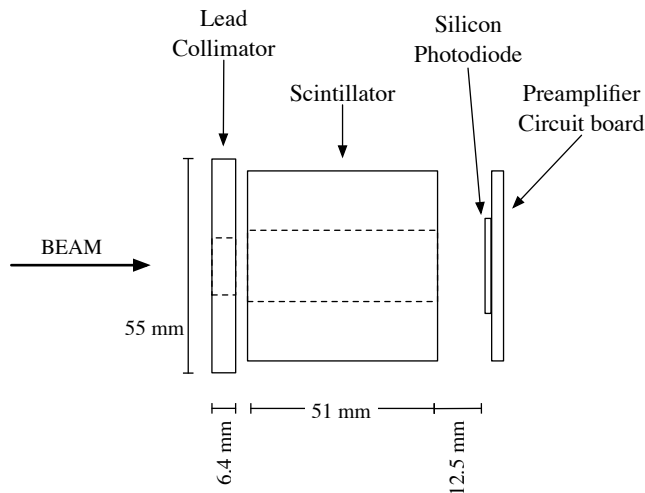


FIG. 1: Schematic of the detector assembly. The various hole diameters are given in the text. The cooled copper mount is not shown, but was located behind the preamplifier circuit board.

tor generated timing signals, which were combined in an OR module, and the resulting logic signal was delayed and used to trigger the data acquisition system (DAQ), contained in a single computer-automated measurement and control (CAMAC) crate. A parallel output of the OR unit was used to stop the TAC, which was started by the signal from the scintillator. This TAC signal was also digitized. Thus any signal over the 30-keV threshold from the silicon detector would trigger the DAQ, while a coincidence (within a 5- μ s time window) would also produce a TAC output. The threshold on the scintillator was set high enough that its rate was substantially lower than that in the silicon diode detector. The DAQ system was operated in event mode, with two silicon detector energy signals, one scintillator pulse height, and one timing signal per event.

A precision pulser, coupled to the silicon detector preamplifier, was used for monitoring dead time and amplifier gain shifts. A scaler module was used to count pulser triggers, pulses from the beam-current integrator, the number of TAC outputs, and the number of DAQ triggers. The pulser and the electronics feeding the DAQ system were located in a temperature-stabilized rack, which was controlled to within $\pm 0.1^\circ\text{C}$. During regular data taking the pulser was set to correspond to about a 0.5 MeV signal in the silicon detector. The DAQ CAMAC crate was located in the temperature-controlled electronics rack and was controlled by a Wiener CC32 peripheral component interconnect (PCI) crate controller [14]. For data acquisition, initially we used the JAVA-based JAM [15] system, but subsequently switched to the Objective-C-based ORCA [16] system.

The gain stability of the silicon-detector preamplifier and associated electronics was monitored by observing the pulser signal in the high- and low-gain channels.

Also, the irradiations were stopped at hourly intervals, and a measurement of the pulser spectrum for various settings of the pulser attenuation circuit was made ($1.0\times, 0.5\times, 0.2\times, 0.1\times$). These measurements allowed for the monitoring of both gain and linearity as a function of irradiation time.

From the event-mode data, singles histograms of the silicon-detector energy spectra, the TAC signals, and the scintillator pulse height were formed. Prompt coincident events were retained by applying cuts (discussed in section III) to the TAC and scintillator spectra.

D. Calibration

1. Silicon detector energy calibration

The energy calibration for the ${}^8\text{B}(2^+) \rightarrow {}^8\text{Be}(0^+)$ decay measurement was obtained from a ${}^{133}\text{Ba}$ radioactive source, which produces a number of low-energy gamma-ray lines between 80–400 keV. These photons convert by Compton scattering and the photoelectric effect in the silicon. In contrast, measurement of the ${}^8\text{B}(2^+) \rightarrow {}^8\text{Be}(0^+)$ decay rate involved the detection of two low-energy alpha particles, which directly ionize the detector medium. The ionization energy for gamma rays in silicon, 3.68 ± 0.02 eV, is larger than the ionization energy for alpha particles in silicon, 3.62 ± 0.02 eV. This difference, a ratio of 1.017 ± 0.008 , must be accounted for when relating a calibration obtained from gamma-rays to the measured alpha-particle energy spectrum [17]. In addition, the fractional loss of energy to non-ionizing processes increases as the alpha particle incident energy decreases; this *pulse-height defect* goes undetected by the silicon detector.

Tabulated values of the expected nuclear and total stopping powers have been published in [18]. At low energies, these tabulated nuclear stopping powers are calculated via a model, as available experimental data are limited. In order to determine the expected pulse height of the ${}^8\text{B}(2^+) \rightarrow {}^8\text{Be}(0^+)$ decay signal reliably, it was necessary to measure the pulse-height defect of alpha particles in our silicon detector.

The uncertainty in the ionization energy ratio affects the determination of the pulse-height defect, but, as will be seen below, the calibration of the low-energy alpha particles is not affected by it. Thus we divide the calibration obtained from ${}^{133}\text{Ba}$ by 1.017 to get the corresponding calibration for alpha particles without the pulse-height deficit, and these energies are used for our calibrations. The pulse-height deficit (with uncertainties) is applied subsequently.

In order to measure the pulse-height defect of low-energy alpha particles in silicon, ${}^4\text{He}$ ions were produced at eight different energies from 90–475 keV using the UW Tandem accelerator with the Terminal Ion Source. These alpha particles were backscattered from a gold monolayer evaporated on a 50- $\mu\text{g}/\text{cm}^2$ carbon target foil into the

collimated silicon detector located at 100 degrees. As the energy the particles deposit in the active part of the detector is reduced from the incident energy by the SiO_2 deadlayer on the front of the detector, it was necessary to quantify the energy loss in the deadlayer. This was done by repeating the measurements for each incident energy with the detector face angled at numerous positions between -45 and $+45$ degrees to the scattering axis. At each angle, the effective thickness of the deadlayer through which the particles passed is $\Delta x / \cos \theta$, where Δx is the physical deadlayer thickness. The value of Δx was determined by combining all of the measured results and performing a global fit to the measured energy (as determined from the ^{133}Ba calibration, adjusted by the ratio of ionization energy for electrons and alpha particles) vs. detector angular position. From this series of experiments, the pulse-height defect was found to vary from 7.9 ± 0.3 to 11.4 ± 0.7 keV for alpha-particle incident energies in the active part of the detector varying from 55.9 to 391.4 keV. The measured energy loss in the deadlayer corresponded to $43.1 \pm 0.4 \mu\text{g}/\text{cm}^2$ of SiO_2 . There is an additional systematic uncertainty of 0.8% in these pulse-height defects, arising from the uncertainty in the ratio of ionization energy for alpha particles to that for photons [17].

The low-energy alpha calibration, including corrections for pulse-height defect and for the ratio of ionization energy for electrons and alpha particles, was cross-checked using the decay of implanted ^{12}N , which beta-decays to the 7.65-MeV state of ^{12}C , which then decays to three alpha particles with a total energy release of 379 keV.

Two of the alpha particles come from the breakup of the ground state of ^8Be . By comparing the known energy of this decay (accounting for decay kinematics, discussed in the following section) to the detected energy deposition, we were able to determine the pulse-height defect independently, assuming that the energy dependence of the pulse-height defect was that given by the predicted non-ionizing stopping power [18]. The spectrum obtained from the ^{12}N decay is shown in Fig. 2. The results of the ^{12}N decay and the single alpha-particle measurements are shown in Fig. 3, along with the predicted pulse-height defect obtained from [18]. The pulse-height defect obtained from the single alpha-particle measurement is calculated to be 7.5 ± 0.3 keV at 46 keV. On the other hand, the pulse-height defect from the ^{12}N decay measurement is found to be 4.5 ± 0.9 keV at 46 keV. We use these two values as lower and upper bounds when constructing the energy window for the expected signature from ^8B decay.

As the low-energy alpha calibration includes corrections for both pulse-height defect and for the ratio of ionization energies, and as the former is obtained using the latter, uncertainties in this ratio will cancel in the calibration for the ^8B measurement. The photons are just an intermediate calibration. The determination of the pulse-height defect links a known alpha-particle energy to a photon energy, and then the use of that photon for calibrating the measurement of ^8B establishes that

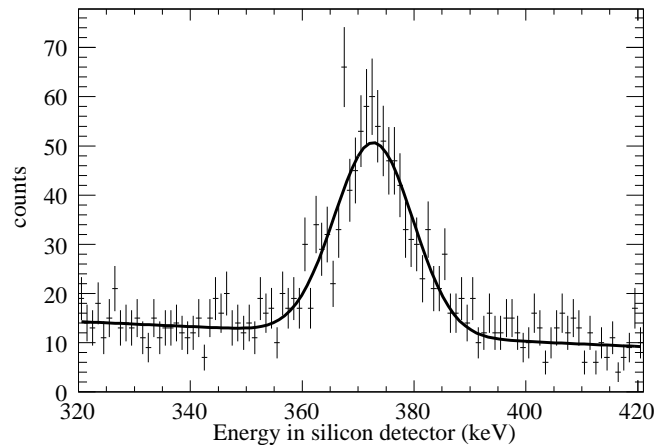


FIG. 2: The ^{12}N 3α decay peak observed in the high gain channel, fit with a Gaussian peak on a linear background. The energy deposited, including recoil and positron summing, is predicted to be 388.5 ± 1.2 keV from our Monte Carlo simulations. The center of the peak appears at 372.5 ± 3.0 keV, indicating a total 16 ± 3 keV pulse-height defect.

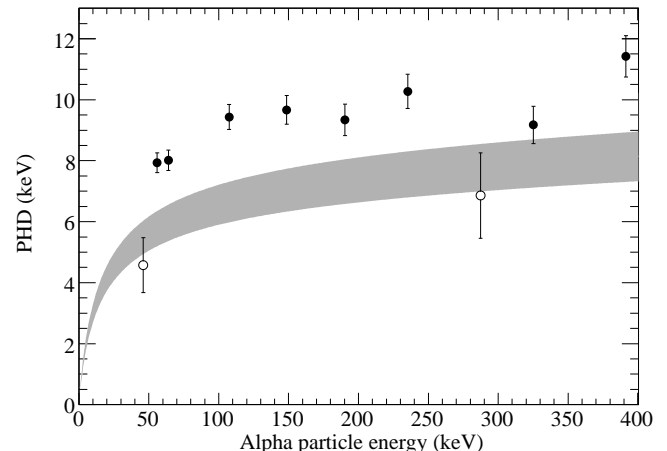


FIG. 3: Pulse-height defect (PHD) measured using single alpha particles (solid circles) and from ^{12}N decay (open circles). The shaded band is the PHD value obtained from integrating the stopping-power tables in [18], including a 10% uncertainty.

calibration in terms the known alpha-particle energy.

The low-gain channel, which contained the $^8\text{B}(2+) \rightarrow ^8\text{Be}(2+)$ decays, was calibrated using the two lines from ^{12}N decay, resulting from the 3α decay of the ^{12}C levels at 7.65 and 12.71 MeV. These are illustrated in Fig. 4. The energies of these lines were adjusted for positron summing, ^{12}C recoil and pulse-height defect.

2. Recoil and energy deposition calculations

Two corrections are required for the analysis of both ^8B and ^{12}N energy spectra: the recoil energy imparted by the leptons to the daughter nucleus, and the amount

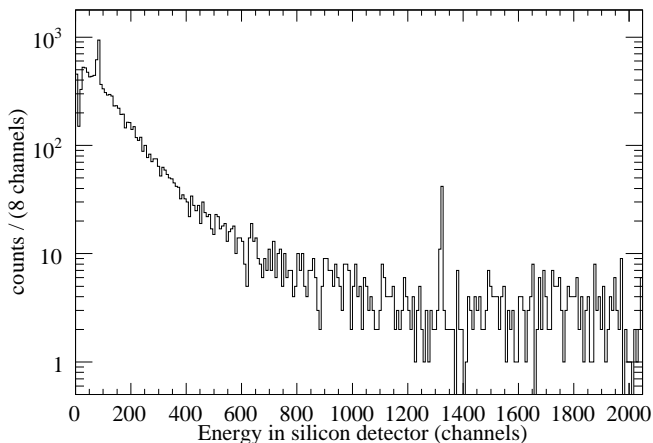


FIG. 4: The ^{12}N spectrum observed in the low-gain channel. The peaks near channels 80 and 1300 correspond to total energies from 3α decay of 388.5 ± 1.2 and 5443 ± 6 keV, respectively, including recoil and positron summing. The continuum is dominated by positrons backscattering from the detector mount and thus passing through the detector twice. In ^{12}N decay, only 3% of the positrons are accompanied by alphas.

of energy deposited in the silicon detector by the outgoing positron. As a result of the high decay energy, a significant amount of recoil energy (up to 19 keV) can be imparted to the ^8Be daughter nuclei by the outgoing leptons, resulting in an overall broadening of the energy window in which the decay signal is expected to lie. The ^{12}C daughters receive less recoil energy (up to 3.3 keV). Using the predictions of the positron-neutrino correlation from the calculations described in Sec. IV, we found a distribution of recoil energy between 0 and 19 keV for the $^8\text{B}(2^+) \rightarrow ^8\text{Be}(0^+)$ decay, which was peaked near the maximum energy. The Gamow-Teller decay of ^{12}N yields a fairly uniform distribution of recoil energy between 0 and 3.3 keV.

The additional energy deposited by the escaping positron adds to the decay energy and results in an overall energy shift. We minimized the magnitude of this energy shift by implanting the ^8B and ^{12}N ions near the upstream surface of the silicon detector. The distribution of the positron energy deposition was computed by Monte-Carlo simulation, using measured stopping powers from [18]. The ^8B and ^{12}N implantation depths, 20.2 ± 0.3 and 18.7 ± 1.5 microns respectively, were obtained from [19]. The simulated energy distributions were fit with a Landau distribution, and the most likely energy deposition for positrons coming from $^8\text{B}(2^+) \rightarrow ^8\text{Be}(0^+)$ and ^{12}N decay was 9.5 ± 0.9 and 7.8 ± 0.6 keV respectively.

A significant number of positrons undergo large angle scattering, in either the silicon or the copper detector mount, before reaching the scintillator and resulting in a coincidence trigger. Their energy deposition in the silicon detector is large enough to remove the event entirely from the expected energy range for the $^8\text{B}(2^+) \rightarrow ^8\text{Be}(0^+)$ decay. As described below, we deter-

mined that positron summing reduced our efficiency for detecting ground state decays by 11.5%.

III. DATA ANALYSIS

Following a series of commissioning runs, we accumulated 2.5×10^6 ^8B decay events over the course of two experimental runs. After selecting prompt events and applying cuts on the amplitude of the pulse in the scintillation counter, 2.0×10^6 events remained. The following discussion applies to both runs and is illustrated by examples from the second.

Following each run, the data in each of the silicon detector channels were corrected for gain drifts (the average correction was less than 0.3%), and the high-gain channel was calibrated using the information from the ^{133}Ba calibration data. A correction was also made for the alpha/gamma ionization energy difference. No adjustments or calibrations were made to the scintillator or TAC spectra. The events of the final data set consisted of the corrected silicon-detector values and the corresponding raw scintillator and TAC values. This processing was applied separately to the data obtained using the ^3He and ^4He target gas. The ratio of random to true coincidence rate, in the energy region where the ground state decay is expected, was found to be approximately 0.5% for both the ^3He and ^4He data. Since these data were subtracted to obtain the final data set, we made no further correction for accidental coincidences.

The spectrum from the low-gain channel, which is dominated by the $^8\text{B}(2^+) \rightarrow ^8\text{Be}(2^+)$ decay, is shown in Fig. 5. Above about 8 MeV, Monte Carlo simulations indicate the spectrum is distorted by alpha particles that escape from the 20- μm implantation depth. Additional small distortions result from the scintillator threshold, which requires positrons over about 1.5 MeV, and consequently favors lower energy alpha particles. Finally, significant distortions result from backscattered positrons, many of which come from the copper cooling mount behind the detector. Presumably as a result of these distortions, which are examined in detail in Ref. [20], we were unable to get a useful R-matrix fit to this spectrum.

To determine the energy window in which the $^8\text{B}(2^+) \rightarrow ^8\text{Be}(0^+)$ decay should be located, we begin by adding the recoil energy, distributed between 0 and 19.3 keV, to the total kinetic energy (91.8 keV) of the two alpha particles arising from ^8Be decay. To calculate the pulse-height defect of these alpha particles, we assume that the total energy is shared equally between the two alpha particles, thus giving a minimum and maximum kinetic energy for each alpha particle of 45.9 keV and 55.6 keV, respectively. The range of the pulse-height defect for these alpha particles was measured to be 4.5–7.5 keV. Thus, before accounting for the positron energy loss, the ground state decay could be expected to appear between 9 and 15 keV lower than the sum of the decay and recoil energies. We convolve the calculated alpha-particle en-

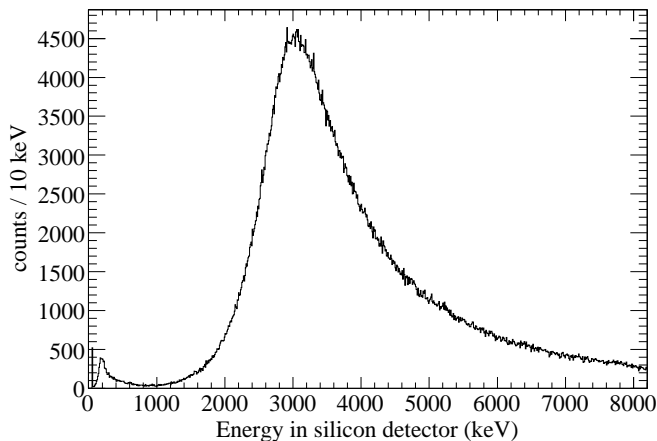


FIG. 5: Spectrum from the low-gain channel of the silicon detector, dominated by the ${}^8\text{B}(2^+) \rightarrow {}^8\text{Be}(2^+)$ decay. As discussed in the text, the $20\text{-}\mu\text{m}$ implantation depth limits the reliability of this spectrum to energies below 8 MeV.

ergy distribution with a Gaussian detector response with the typical 9-keV FWHM to produce an expected energy spectrum. The pulse height defect shifts this spectrum downward between 9 and 15 keV. For each of these cases we convolve the shifted spectrum with the spectrum of positron energy deposition calculated using the PENELOPE Monte-Carlo package [21]. That spectrum corresponds to positrons emitted isotropically but depositing over 2.5 MeV in the scintillator. The spectrum has a peak at about 9 keV, corresponding to positrons that exited the silicon in the direction of the scintillator, but there is a long tail produced by positrons that either backscattered from the copper mount or that passed through significant thickness of silicon before a large-angle scattering into the scintillator. The final spectra, for the two limiting values of pulse height defect, including positron summing, are illustrated in Fig. 6. We select the energy range from 75 to 120 keV for the region of interest. This region contains between 88.1% and 88.8% of the total events, depending on the assumed value for the pulse height defect.

In this energy window the rates of the two background processes in ${}^8\text{Be}$, gamma-decay of excited states of ${}^8\text{Be}$ and alpha particles from the broad ${}^8\text{B}(2^+) \rightarrow {}^8\text{Be}(2^+)$ decay spectrum, were calculated to be two orders of magnitude below the sensitivity of this experiment.

The spectra obtained in the second experimental run, with ${}^3\text{He}$ (signal) and ${}^4\text{He}$ (background) in the gas cell, are shown in Fig. 7. The most striking feature is the large broad peak of coincident events, which was present in our data regardless of the target gas, and (at a slightly lower rate) even without the beam. The rate of events in this peak, 20 mHz, was relatively constant over a long time span (~ 4 years), regardless of the time between irradiations in the scattering chamber. We speculate that this peak is due to minimum-ionizing events from ambient radioactivity which pass through both the silicon

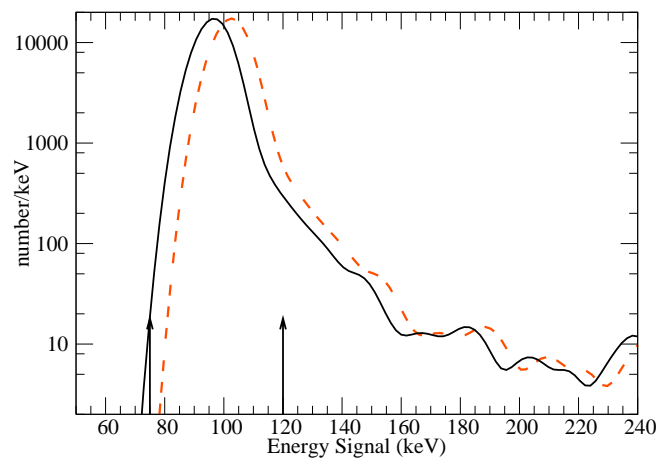


FIG. 6: Monte Carlo simulations of silicon detector response to decays to the ${}^8\text{Be}$ ground state for coincident events in scintillator and Si detectors. The initial alpha-particle energy spectrum is modified by recoil and positron energy summing. The two curves correspond to the two extreme values for the pulse height defect. The arrows indicate the region chosen for searching for ground state decays.

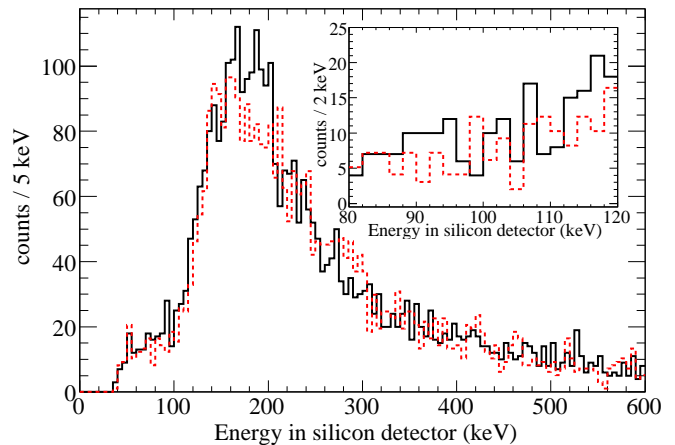


FIG. 7: Measured signal (solid) and background (dashed) coincidence silicon-detector spectra for the high-gain channel with scintillator threshold applied.

and scintillator detectors. However, increased shielding and the addition of scintillator veto counters were not effective in reducing the rate.

Analysis of these events shows that they are dominated by low-energy scintillator events, and we can improve our experimental sensitivity by optimizing the scintillator minimum threshold. The optimum scintillator threshold was obtained by finding the minimum uncertainty in the difference of the time-normalized signal and background counts between 75 – 120 keV as a function of scintillator threshold. We maintained the average beam current in the measurements with ${}^3\text{He}$ and ${}^4\text{He}$ to be identical within 1%, so normalizing by time was equivalent to normalizing by integrated current. We subtracted the nor-

malized background given by the ^4He data from the ^3He data.

Along with the background discussed above, there was additional background present in the spectrum measured using the signal ($^6\text{Li} + ^3\text{He}$) reaction which was not present in the background ($^6\text{Li} + ^4\text{He}$) measurement. We hypothesize that this additional background resulted from positrons emitted from ^8B implanted on surfaces other than the silicon detector. These positrons may pass through both the silicon and scintillator detectors and result in a false coincidence trigger and a continuum of events in the energy spectrum.

Since this background had the same general shape as the larger background observed with the beam off or with ^4He in the gas cell, we assume it is composed primarily of a spectrum of the same shape, but we will allow for the possibility of additional background in the energy range of interest. Such a background would be identified by additional counts in the spectrum adjacent to the energy window for the ground state decay.

In order to account for the first part of this background, we parameterized the shape of the background spectrum by fitting the measured background energy spectrum from 50–400 keV, as shown in the first plot of Fig. 8. The parameterization function consisted of a Landau distribution and a linear term. Holding the parameters from the background fit fixed and allowing for a free multiplicative normalization factor, the parameterization function was then fit to the signal energy spectrum over an energy window from 140 – 400 keV, as shown in the second plot of Fig. 8. Excluding the area around the $^8\text{B}(2^+) \rightarrow ^8\text{Be}(0^+)$ decay signature window ensures that the normalization was not influenced by counts in that window. The number of expected background events in the signal region was obtained by integrating the fit function over the energy region of interest. In order to identify the second part of this background, the excess of counts above this calculated background was computed in the signal window (75 – 120 keV) and two adjacent energy windows (50 – 75 keV and 120 – 140 keV).

The excess of net counts above the fit background in all three energy windows confirms the second background, which is not present in the ^4He measurements from which the initial background estimates are derived. To account for this additional background, we interpolated between the two adjacent windows to determine the number of background events in the primary energy window. We then subtracted this background from the total number of excess events obtained from the difference between the data and the fit, to get the net excess of signal events. To account for the loss of efficiency due to positron backscattering, we multiplied the net excess of counts by 1.13. The branching ratio was calculated by dividing the corrected net excess number of counts by the total number of detected coincident events. The results of this analysis are given in Table I.

The data from the two experimental runs, given in table I, combined with the total of 1.96×10^6 decays col-

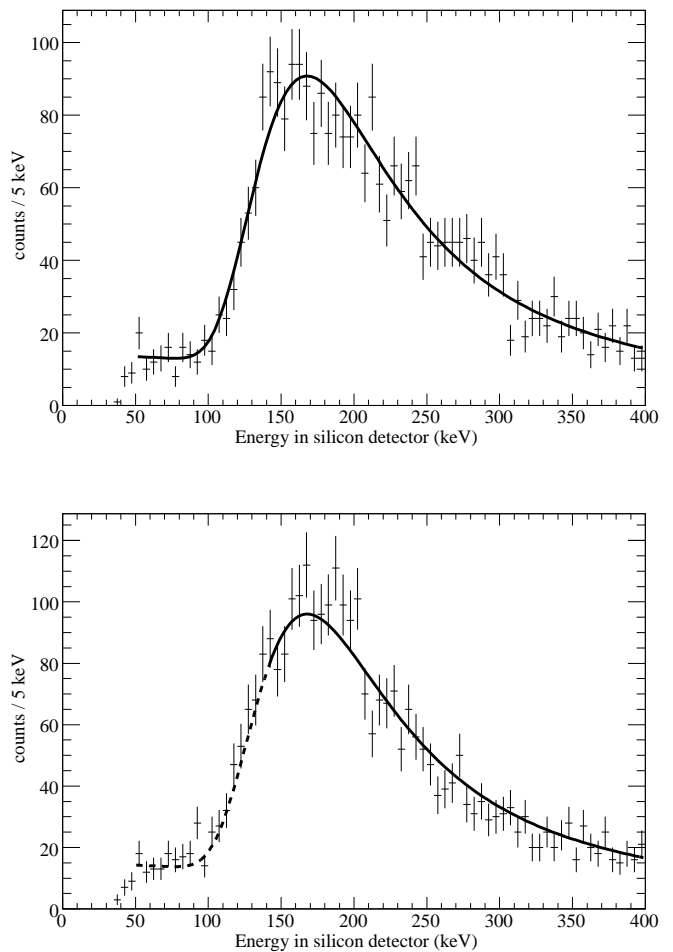


FIG. 8: Data from the second experimental run. The top plot is the data measured with ^4He in the gas cell, with the fit to this background. The bottom plot is the data measured with ^3He in the gas cell, with a fit to the data above 140 keV using the parameters obtained from the background spectrum, but allowing for an adjustable multiplicative normalization. The dashed range of the second curve denotes the energy region of interest for signal extraction.

lected, yields a branching ratio for the $^8\text{B}(2^+) \rightarrow ^8\text{Be}(0^+)$ decay of $(2.6 \pm 3.3) \times 10^{-5}$. This result is consistent with no measured signal and corresponds to an upper limit on the branching ratio of 7.3×10^{-5} at a 90% confidence level.

IV. THEORETICAL ESTIMATE OF BRANCHING RATIO

One published estimate [6, 7] of the $^8\text{B}(2^+) \rightarrow ^8\text{Be}(0^+)$ decay rate is based on conserved vector current (CVC), which relates the vector contribution to the beta-decay rate to the gamma decay of the 16-MeV isobaric analogue state of ^8Be [22]. These calculations do not consider the contribution of the axial matrix element to the decay

TABLE I: Number of measured events and predicted background in the spectrum obtained with ^3He gas in the cell. Both experimental runs are combined.

energy window (keV)	events from data	bkg. events from fit	net remaining	interpolated bkg.	net excess
50–75	282 ± 16.8	255.7 ± 16.0	26.2 ± 23.2	—	—
75–120	661 ± 25.7	575.4 ± 24.0	85.6 ± 35.2	40.4 ± 44.4	45.2 ± 56.7
120–140	589 ± 24.2	573.9 ± 23.8	15.1 ± 34.0	—	—

rate. Another estimate [5] is based on several different model calculations of the axial-vector second-forbidden contribution to the decay to the first excited state of ^8Be . Those authors suggest that, based on the similarity of the intrinsic wave functions of the ground and first excited states of ^8Be , these calculations can be applied to the ground state decay, and they find a branching ratio of approximately 3×10^{-6} . However, since there is no experimental information available to constrain the contribution of the axial matrix element to the transition, a strong axial contribution cannot simply be ruled out.

In this section, we discuss our application of the framework developed by Walecka [23, 24] and Donnelly and Haxton [25] for calculating the rates of electromagnetic and semileptonic processes. The details of the calculations discussed in this section are specific to the $^8\text{B}(2^+) \rightarrow ^8\text{Be}(0^+)$ decay. Our application of this framework is described in detail in Ref. [20].

A. Shell model estimate

The rate of the $^8\text{B}(2^+) \rightarrow ^8\text{Be}(0^+)$ second-forbidden ^8B decay can be expressed in terms of kinematic variables and multipole matrix elements, using the formalism in [23]. This formalism is quite general, as it includes all multipoles and leaves the local weak current unspecified – so that exchange-current or other corrections to the usual one-body operators can be included. The transition of interest involves an angular momentum change from $J=2$ to $J=0$, with no change in parity. The relevant operators, expanded in the long-wavelength limit (since $qR \ll \hbar c$), are given in terms of the vector and axial vector currents, $\mathbf{J}(\mathbf{x})$ and $\mathbf{J}_5(\mathbf{x})$ [24]. These operators, $\hat{M}_2(q)$, $\hat{T}_2^{\text{el}}(q)$, and $\hat{T}_2^{\text{mag}5}(q)$, are the rank-two charge and transverse electric projections of the vector current and the transverse magnetic projection of the axial current, respectively.

The vector current appearing in \hat{T}_2^{el} has a one-body part and two-body exchange-current corrections, both of which are of the order (v_{nuc}/c) . A direct calculation of the important exchange current corrections would be difficult to do precisely in a model calculation. Fortunately, under CVC and in the long wavelength limit, it is possible to rewrite matrix elements of \hat{T}_2^{el} in terms of those of \hat{M}_2 through Siegert’s Theorem [26]. The benefit of this substitution is that the one-body charge operator is of order $(v_{\text{nuc}}/c)^0$, while two-body corrections to this operator

are of order $(v_{\text{nuc}}/c)^2$. Thus Siegert’s theorem allows one to deal with a simpler operator that can be well approximated by its one-body form. The beta-decay rate then can be written in terms of $\hat{M}_2(q)$ and $\hat{T}_2^{\text{mag}5}(q)$. As discussed below, the matrix element of the Coulomb operator can be taken from the isobaric analogue gamma decay transition. Thus the nuclear-structure dependence of our result is effectively isolated in a single matrix-element ratio, $\langle \hat{T}_2^{\text{mag}5} \rangle / \langle \hat{M}_2 \rangle$.

B. Calculation of the density matrix

For weak and electromagnetic interactions, the interaction can be well-approximated by considering only the one-body interaction [25]. We define $|\alpha\rangle$ and $|\beta\rangle$ as complete single-particle wavefunctions, and we also define $||\alpha\rangle$ and $||\beta\rangle$ as the reduced (in angular momentum and isospin) forms of these single-particle wavefunctions, i.e. $|n, l, j, t\rangle$. We can then write a many-body multipole reduced matrix element $\langle J_f T_f || \hat{\mathcal{O}}_{JT} || J_i T_i \rangle$ as the sum of single particle matrix elements $\langle \alpha || \mathcal{O}_{JT} || \beta \rangle$ multiplied by the density matrix elements $\psi_{\alpha\beta}$, as defined in [25]

For the $^8\text{B}(2^+) \rightarrow ^8\text{Be}(0^+)$ transition, the coefficients for the density matrix were obtained from p-shell wavefunctions calculated using the GLASGOW shell-model [27] with the Cohen-Kurath (8-16)2BME interaction [28]. The numerical values are given in Table II.

TABLE II: Calculated density matrix elements for 1p-shell transitions for $^8\text{B}(2^+) \rightarrow ^8\text{Be}(0^+)$ decay, using the Cohen-Kurath (8-16)2BME interaction [28] and calculated using code obtained from [29]. The notation $a \rightarrow b$ denotes the density matrix element ψ_{ab} , which connects the single particle states with $j_i = a$ and $j_f = b$.

transition	density matrix coefficient
$\frac{1}{2} \rightarrow \frac{3}{2}$	-0.206564
$\frac{3}{2} \rightarrow \frac{1}{2}$	+0.168713
$\frac{3}{2} \rightarrow \frac{3}{2}$	-0.608563

C. Single-particle matrix elements

The single-particle operators relevant to this calculation are defined in terms of spherical Bessel functions

j_J and scalar and vector spherical harmonics $Y_J^{M_J}$ and $\mathcal{Y}_{JL1}^{M_J}$ [25]:

$$M_J^{M_J}(\mathbf{q}\mathbf{x}) \equiv j_J(qx)Y_J^{M_J}(\Omega_x), \quad (1)$$

$$\Sigma_J^{M_J}(\mathbf{q}\mathbf{x}) \equiv j_J(qx)\mathcal{Y}_{JJ1}^{M_J}(\Omega_x) \cdot \boldsymbol{\sigma}. \quad (2)$$

The matrix elements of these operators can be expanded in a harmonic oscillator basis and expressed as functions of the form [25]:

$$\langle n_f(l_f \frac{1}{2})j_f \| T_J(\mathbf{q}\mathbf{x}) \| n_i(l_i \frac{1}{2})j_i \rangle = \sqrt{\frac{1}{4\pi}} y^{(J-2)/2} e^{-y} p(y), \quad (3)$$

where $T_J(\mathbf{q}\mathbf{x})$ is a generic single-particle operator reduced in spin/isospin, $y \equiv (\frac{1}{2}qb)^2$, $b=1.787$ fm is the oscillator parameter [30], and $p(y)$ is a polynomial of finite order in y , as tabulated in [25].

Folding the matrix elements of [25] with the Cohen-Kurath density matrix yields

$$\langle J_f \| \hat{M}_2 \| J_i \rangle = \frac{-0.23F_1}{\sqrt{4\pi}} \left(-\frac{4y}{3} \right) \exp(-y), \quad (4a)$$

$$\langle J_f \| \hat{T}_2^{\text{mag}5} \| J_i \rangle = \frac{0.04F_A\sqrt{6}}{\sqrt{4\pi}} \left(-\frac{2y}{3} \right) \exp(-y), \quad (4b)$$

where $F_1 = 1.0$ and $F_A = 1.26$ are the single-nucleon charge and axial-vector couplings.

While the \hat{M}_2 and $\hat{T}_2^{\text{mag}5}$ matrix elements have identical momentum dependence, a suppression of the $\hat{T}_2^{\text{mag}5}$ matrix element is caused by the cancelation to 20% in the sum of the density matrix elements:

$$\psi_{\frac{3}{2}\frac{3}{2}} + \psi_{\frac{1}{2}\frac{3}{2}} = 0.17 - 0.21 = -0.04. \quad (5)$$

The uncertainty of this model dependence is difficult to quantify, and therefore we unfortunately cannot be assured that this result reflects the true strength of the axial contribution to this decay. Despite this, we are now able to obtain the beta decay rate for the ${}^8\text{B}(2^+) \rightarrow {}^8\text{Be}(0^+)$ decay. We find that the vector contribution dominates, and the resulting branching ratio is 6.1×10^{-5} .

D. Vector contribution derived from electromagnetic rate

Since our shell model calculation showed dominance of the vector contribution to the decay, it is useful to compare that result with the value implied by measurements of isobaric analogue electromagnetic transitions. The doublet in ${}^8\text{Be}$ at 16.6/16.9 MeV is composed of a $T = 0$ state mixed with the $T = 1$ isobaric analogue state of the ${}^8\text{B}$ ground state. The reduced strengths for the E2 transition from these states to the ground state of ${}^8\text{Be}$ are $B(E2)_{16.6} = 0.068 \pm 0.024 e^2 \text{fm}^4$ and $B(E2)_{16.9} = 0.075 \pm 0.013 e^2 \text{fm}^4$ [22]. Due to ambiguity in the phase of the matrix elements, decomposing the measured transition strengths into isovector and

isoscalar components gives two results: either $B(E2)_{\text{IV}} = 0.00 \pm 0.03 e^2 \text{fm}^4$ and $B(E2)_{\text{IS}} = 0.14 \pm 0.03 e^2 \text{fm}^4$, or alternatively, $B(E2)_{\text{IV}} = 0.14 \pm 0.03 e^2 \text{fm}^4$ and $B(E2)_{\text{IS}} = 0.00 \pm 0.03 e^2 \text{fm}^4$. We will henceforth use the maximum ($0.14 + 0.03 = 0.17 e^2 \text{fm}^4$) and minimum (0.0) values for $B(E2)_{\text{IV}}$ to constrain the beta decay transition rate.

The rate of the nuclear electromagnetic transition rate in terms of the multipole operators defined in the previous section is [24],

$$\omega_\gamma = \frac{8\pi\alpha k_\gamma}{2J_i + 1} |\langle f \| \hat{T}_J^{\text{el}} \| i \rangle|^2, \quad (6)$$

where ω_γ is the transition rate per unit time, k_γ is the gamma-ray momentum, α is the fine structure constant, J is the angular momentum change in the transition, and J_i is the initial spin of the nucleus. As with the beta decay expression, we can rewrite this in terms of the \hat{M}_2 matrix element using Siegert's Theorem [26] and substituting $J = J_i = 2$,

$$\omega_\gamma = \frac{3}{2} \frac{8\pi\alpha}{5} \frac{(E_i - E_f)^2}{k_\gamma} |\langle f \| \hat{M}_2 \| i \rangle|^2. \quad (7)$$

The energy released in the isovector decay is 16.80 MeV [22], and the corresponding decay rate from Eq. 7 yields a $B(E2)$ value of $0.55 e^2 \text{fm}^4$ for the transition, using the \hat{M}_2 matrix element obtained in the previous section. In order for this calculation to match the measured $B(E2) = 0.17 e^2 \text{fm}^4$, the matrix element must be reduced by a factor of 1.8. To incorporate the second ($B(E2)_{\text{IV}} = 0$) constraint, we simply set $M_2 = 0$ in the beta decay calculation.

If we assume the maximum possible strength of the vector matrix element from the gamma decay measurement, we obtain a transition rate of $1.8 \times 10^{-5} \text{s}^{-1}$. On the other hand, if we assume that the vector matrix element does not contribute, the transition rate is reduced to $9.1 \times 10^{-7} \text{s}^{-1}$. The respective branching ratios for these cases are 2.0×10^{-5} and 1.0×10^{-6} .

V. CONCLUSIONS

An accurate measurement of or limit on the ${}^8\text{B}(2^+) \rightarrow {}^8\text{Be}(0^+)$ beta decay branching ratio is of importance for the current generation of solar neutrino measurements. To the best of our knowledge, this work is the first published attempt at the measurement of the ${}^8\text{B}(2^+) \rightarrow {}^8\text{Be}(0^+)$ decay branching ratio.

Our measurement of the ${}^8\text{B}(2^+) \rightarrow {}^8\text{Be}(0^+)$ beta decay transition centers on the detection of the two low-energy alpha particles from the breakup of ${}^8\text{Be}$. A significant challenge to this measurement is the characterization of the response of our silicon detector to low-energy alpha particles. In light of this, we have done two experiments to determine our detector response. The first measurement involved directly implanting alpha particles with kinetic energy between 86 and 453 keV into our detector,

while simultaneously measuring the detector deadlayer. The second measurement involved the implantation of ^{12}N , which is unstable to beta-delayed 3α decay. The results from both of these measurements verify that the tabulated nuclear stopping powers for alpha particles in silicon are reasonably valid for the range of energies we are considering. However, the directly-implanted low-energy alpha particle measurements indicates that the uncertainty on the tabulated values may be larger than predicted.

Using the measurements and techniques described above, we have measured the ${}^8\text{B}(2^+) \rightarrow {}^8\text{Be}(0^+)$ decay branching ratio to be $(2.6 \pm 3.3) \times 10^{-5}$. This measurement is consistent with zero and can be used to place an upper limit on the branching ratio of 7.3×10^{-5} at the 90% confidence level. At this level, the ${}^8\text{B}(2^+) \rightarrow {}^8\text{Be}(0^+)$ decay branch is not a significant background to measurements of the spectral shape of solar ${}^8\text{B}$ neutrinos and the solar hep neutrino flux. Our calculation of the ${}^8\text{B}(2^+) \rightarrow {}^8\text{Be}(0^+)$ decay rate gives a branching ratio of 6.1×10^{-5} , using values for the vector and axial-vector matrix elements obtained from the shell model. The model-dependent axial term in our calculation may be quite uncertain. We find a branching ratio range of

1.0×10^{-6} to 2.0×10^{-5} , based on the values for the vector matrix element obtained from the experiment of Ref. [22] along with the axial-vector matrix element obtained from the shell model. The values are all consistent with our measured value.

Acknowledgments

The authors would like to thank Wick Haxton for his assistance with the theoretical aspects of this work. The CENPA technical staff: John Amsbaugh, Greg Harper, Mark Howe, and Doug Will, also contributed extraordinary amounts of time and effort in support of the experimental measurements. We also wish to thank Eric Adelberger, Manojet Bhattacharya, Jason Detwiler, Alejandro Garcia, Seth Hoedl, and John Wilkerson for their wealth of ideas and insights. Finally, work by Matthias Gohl, Shuje Uehara, Ashley Batchelor, Christy McKinley, Patrick Peplowski and many other UW Tandem crew members, was crucial to carrying out this work. This research was partially supported by DOE Grant DE-FG03-97ER41020.

-
- [1] W. T. Winter, S. J. Freedman, K. E. Rehm, and J. P. Schiffer, *Phys. Rev. C* **73**, 025503 (2006).
- [2] M. Bhattacharya, E. G. Adelberger, and H. E. Swanson, *Phys. Rev. C* **73**, 055802 (2006).
- [3] C. E. Ortiz, A. Garcia, R. A. Waltz, M. Bhattacharya, and A. K. Komives, *Phys. Rev. Lett.* **85**, 2909 (2000).
- [4] B. Aharmim et al. (SNO), *Astrophys. J.* **653**, 1545 (2006).
- [5] R. Tribble and G. Garvey, *Phys. Rev. C* **12**, 967 (1975).
- [6] C. E. Ortiz, Ph.D. thesis, University of Notre Dame (2000).
- [7] A. Garcia, private communication, confusion of units in a quoted equation caused an error of 10^{-6} in the estimate given in Ortiz' Ph.D. thesis.
- [8] Hamilton Precision Metals, URL www.hpmetals.com.
- [9] U. Rohrer, PSI Graphic Transport Framework based on a CERN-SLAC- FERMILAB version by K.L. Brown et al., URL http://people.web.psi.ch/rohrer_u/trans.htm.
- [10] U. Rohrer, PSI Graphic Turtle Framework based on a CERN-SLAC-FERMILAB version by K.L. Brown et al., URL http://people.web.psi.ch/rohrer_u/turtle.htm.
- [11] J. F. Amsbaugh, G. C. Harper, A. W. Myers, T. D. Van Wechel, and D. I. Will, CENPA Annual Report p. 88 (2005).
- [12] Hamamatsu, URL <http://jp.hamamatsu.com/en/index.html>.
- [13] H. P. Mumm, A. Garcia, L. Grout, M. A. Howe, L. P. Parazzoli, R. G. H. Robertson, K. M. Sundqvist, J. F. Wilkerson, S. J. Freedman, B. K. Fujikawa, et al., *Rev. Sci. Instrum.* **75**, 5343 (2004).
- [14] WIENER, Plein & Baus, Ltd., URL <http://www.wiener-us.com/cc32.htm>.
- [15] D. Visser and K. Swartz, *Jam data acquisition system*, URL <http://sourceforge.net/projects/jam-daq>.
- [16] M. A. Howe, G. A. Cox, P. J. Harvey, F. McGirt, K. Rielage, J. F. Wilkerson, and J. M. Wouters, *IEEE Trans Nucl Science* **51**, 874 (2004).
- [17] ICRU, Tech. Rep. 31, International Commission on Radiation Units, 7910 Woodmont Ave., Washington, DC 20014 (1979).
- [18] M. J. Berger, J. S. Coursey, M. A. Zucker, and J. Chang, *ESTAR, PSTAR, and ASTAR: Computer programs for calculating stopping-power and range tables for electrons, protons, and helium ions*, [online] (2005), an online database with machine-readable stopping power data from ICRU Technical Report 49 (1993), URL <http://physics.nist.gov/Star>.
- [19] J. F. Ziegler, *SRIM: Stopping and Ranges of Ions in Matter*, URL www.srim.org.
- [20] M. K. Bacrania, Ph.D. thesis, University of Washington (2006).
- [21] J. Sempau, E. Acosta, J. Baro, J. M. Fernández-Varea, and F. Salvat, *Nucl. Instrum. Meth.* **B132**, 377 (1997).
- [22] L. De Braekeleer et al., *Phys. Rev. C* **51**, 2778 (1995).
- [23] J. D. Walecka, in *Muon Physics*, edited by V. W. Hughes and C. S. Wu (Academic Press, New York, 1975), vol. II, chap. 2, pp. 113–218.
- [24] J. D. Walecka, *Theoretical Nuclear and Subnuclear Physics* (World Scientific and Imperial College Press, 2004), 2nd ed.
- [25] T. W. Donnelly and W. C. Haxton, *Atomic Data and Nuclear Data Tables* **23**, 103 (1979).
- [26] A. J. F. Siegert, *Phys. Rev.* **52**, 787 (1937).
- [27] R. R. Whitehead, A. Watt, B. J. Cole, and I. Morrison, *Adv. Nucl. Phys.* **9**, 123 (1977).
- [28] S. Cohen and D. Kurath, *Nucl. Phys.* **73**, 1 (1965).

[29] W. C. Haxton, private communication.

[30] J. Dubach and W. C. Haxton, *Phys. Rev. Lett.* **41**, 1453

(1978).